22

Thermal Treatment of Granulated Particles by Induction Thermal Plasma

M. Mofazzal Hossain[1] and Takayuki Watanabe[2]
[1]*Department of Electronics and Communications Engineering, East West University*
[2]*Department of Environmental Chemistry and Engineering*
Tokyo Institute of Technology,
[1]*Bangladesh*
[2]*Japan*

1. Introduction

After the invention of induction plasma torch by [Reed, 1961], tremendous achievements have been earned by the researchers in the field of thermal treatment of micro particles by induction plasma torch. Induction thermal plasma (ITP) has become very popular in material processing due to several of its inherent characteristics: such as contamination free (no electrode), high thermal gradient (between torch and reaction chamber), wide pressure range and high enthalpy. ITP have extensively been used for the synthesis and surface treatment of fine powders since couple of decades as a clean reactive heat source [Fan, 1997], [Watanabe, 2004]. ITP technology may ensure essentially the in-flight one-step melting, short melting time, and less pollution compared with the traditional technologies that have been using in the glass industries for the vitrification of granulated powders. Moreover ITP technology may be very effective in the thermal treatment of porous micro particles and downsizing the particle size. During in-flight treatment of particles, it is rear to have experimental records of thermal history of particles; only some diagnosis of the quenched particles is possible for the characterization. Thus, the numerical analysis is the only tool to have comprehensive characterization of the particle thermal history and energy exchange during in-flight treatment. Thus, for numerical investigation it is the challenge to predict the trajectory and temperature history of the particles injected into the ITP torch. Among others Yoshida et al [Yoshida, 1977] pioneered the modeling of particle heating in induction plasmas; though their work assumed the particle trajectory along the centerline of the torch only. Boulos [Boulos, 1978] developed a model and comprehensively discussed the thermal treatment of alumina powders in the fire ball of argon induction plasma. Later (Proulx et al) [Proulx, 1985] predicted the trajectory and temperature history of alumina and copper particles injected into ITP torch and discussed the particle loading effects in argon induction plasma.
In this chapter we shall discuss the in-flight thermal treatment mechanism of soda-lime-silica glass powders by ITP and to optimize the plasma discharge parameters, particle size and feed-rate of input powders that affect the quenched powders size, morphology, and compositions. The thermal treatment of injected particles depends mainly on the plasma-particle heat transfer efficiency, which in turn depends to a large extent on the trajectory and temperature history of the injected particles. To achieve that goal, a plasma-particle interaction model has been developed for argon-oxygen plasma, including a nozzle inserted

into the torch for the injection of carrier gas and soda-lime-silica glass powders. This model can be used to demonstrate the particle loading effects and to optimize the parameters that govern the particles trajectory, temperature history, quenched particles size and plasma-particle energy exchange efficiency. This model may be used to optimize the plasma and particle parameters for any combination of plasma gases for example argon-oxygen or argon nitrogen etc.

2. Modeling

2.1 Plasma model

The schematic geometry of the ITP torch is presented in Fig.1. The torch dimensions and discharge conditions are tabulated in Table 1. The overall efficiency of the reactor is assumed to be 50%, thus, plasma power is set to 10 kW. The torch dimension, power and induction frequency may vary and can be optimized through the simulation. The model solves the conservation equations and vector potential form of Maxwell's equations simultaneously under LTE (local thermodynamic equilibrium) conditions, including a metal nozzle inserted into the torch. It is assumed that plasma flow is 2-dimensioanl, axi-symmetric, laminar, steady, optically thin, and electromagnetic fields are 2-dimensional. Adding the source terms to the conservation equations, the plasma-particle interaction and particle loading effects have been taken into account. In this model, the conservation equations are as follows:
Mass conservation:

$$\nabla \cdot \rho \mathbf{u} = S_p^C \tag{1}$$

Momentum conservation:

$$\rho \mathbf{u} \cdot \nabla \mathbf{u} = -\nabla p + \nabla \cdot \mu \nabla \mathbf{u} + \mathbf{J} \times \mathbf{B} + S_p^M \tag{2}$$

Distance to initial coil position (L_1)	19 mm
Length of injection tube (L_t)	52 mm
Distance to end of coil position (L_2)	65 mm
Torch length (L_3)	190 mm
Coil diameter (d_c)	5 mm
Wall thickness of quartz tube (T_{wall})	1.5 mm
Inner radius of injection tube (r_1)	1 mm
Outer radius of injection tube (r_t)	4.5 mm
Outer radius of inner slot (r_2)	6.5 mm
Inner radius of outer slot (r_3)	21.5 mm
Torch radius (r_0)	22.5 mm
Coil radius (r_c)	32 mm
Plasma power	10 kW
Working frequency	4 MHz
Working pressure	0.1 MPa
Flow rate of carrier gas (Q_1)	4 ~ 9 L/min of Argon
Flow rate of plasma gas (Q_2)	2 L/min of Argon
Flow rate of sheath gas (Q_3)	22 L/min Argon & 2 L/min Oxygen

Table 1. Torch dimensions & discharge conditions

Energy conservation:

$$\rho \mathbf{u} \cdot \nabla h = \nabla \cdot \left(\frac{\kappa}{C_p} \nabla h \right) + \mathbf{J} \cdot \mathbf{E} - Q_r - S_p^E \tag{3}$$

Species conservation:

$$\rho \mathbf{u} \cdot \nabla y = \nabla \cdot \left(\rho D^m \nabla y \right) + S_p^C \tag{4}$$

Vector potential form of Maxwell electromagnetic field equation [Mostaghimi, 1998]:

$$\nabla^2 \mathbf{A_c} = i \mu_0 \sigma \omega \mathbf{A_c} \tag{5}$$

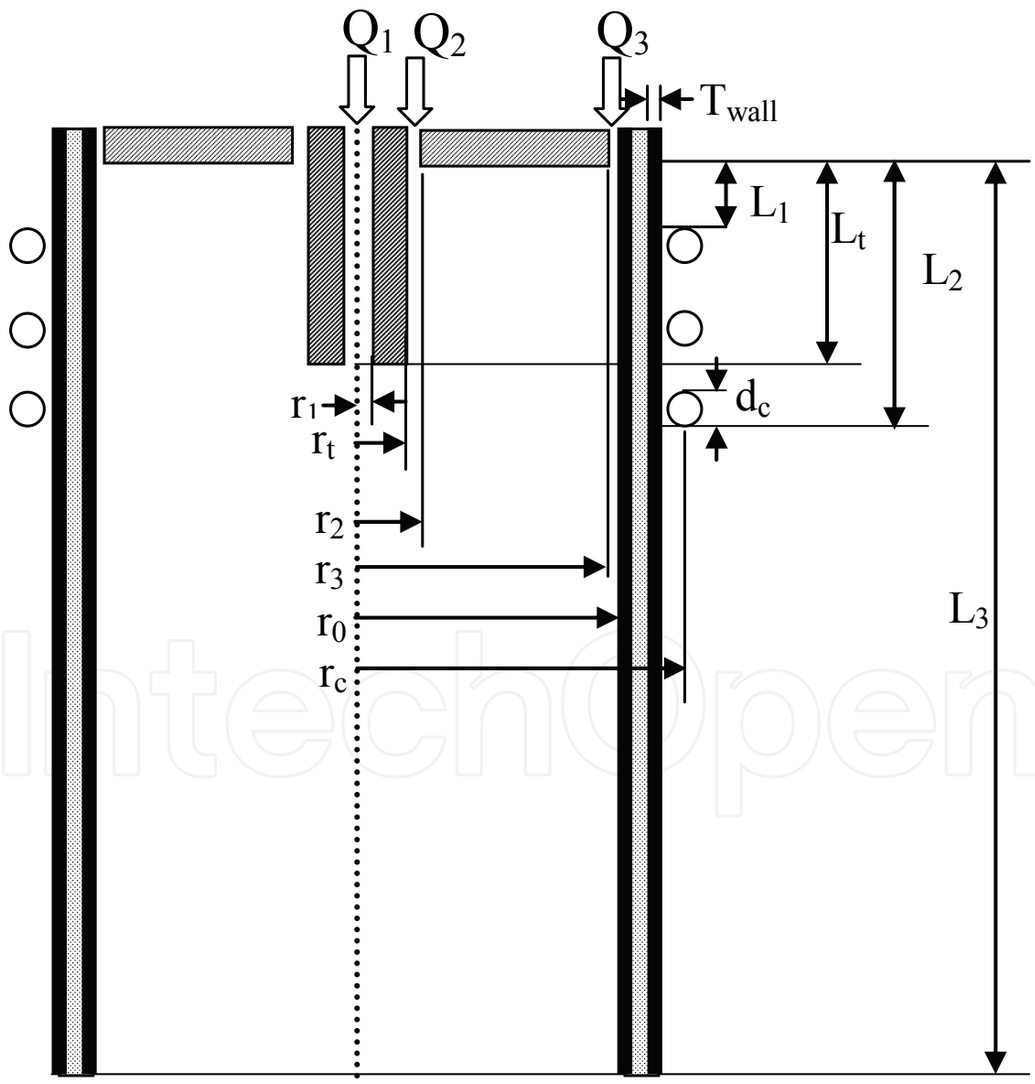

Fig. 1. Schematic geometry of induction thermal plasma torch

2.1.1 Boundary conditions

The boundary conditions for the mass, momentum, energy and species conservation equations are: at the inlet, gas temperature was set to 300 K and uniform velocity profiles are assumed based on the given flow rates; on the axis of symmetry, the symmetry conditions are imposed; on the walls, no-slip condition is assumed; the outer wall temperature is set to 350 K; and, at the exit, axial gradients of all fields are set equal to zero. The inserted nozzle is assumed to be water cooled at 300 K. On the nozzle wall, the velocity is set to zero. The boundary conditions for the vector potential form of Maxwell's equation are the same as those described in reference [Mostaghimi, 1998].

2.1.2 Computational procedure and thermophysical properties

The conservation equations, which are listed in previous section, are solved numerically using the SIMPLER algorithm of Patankar [Patankar, 1980]. The algorithm is based on a control-volume finite-difference scheme for solving the transport equations of incompressible fluids. Calculations are performed for a 44 (in radial direction) by 93 (in axial direction) non-uniform grid system.

Thermodynamic and transport properties of argon and oxygen gases required for the simulation are mass density, specific heat at constant pressure, viscosity, electrical and thermal conductivity and radiative loss coefficient. The transport properties, which are function of temperature, are calculated under LTE conditions using Chapman-Enskog first approximation to Boltzmann equation [Tanaka, 2000]. The effective diffusion coefficient of species is calculated based on the following equations:

$$D_i^m = \frac{\left(1 - y_i\right)}{\sum_{j \neq i, j=1}^{\upsilon} \frac{x_i}{D_{ij}}} \tag{6}$$

$$D_{ij} = 2.628 \times 10^{-2} \sqrt{\frac{\left(M_i + M_j\right)}{2 M_i M_j}} \frac{T^{1.5}}{\bar{\Omega}_{ij}^{(1.1)}} \tag{7}$$

The ambipolar diffusion coefficient for ions can be approximated as $D_a = D_{ion}\ (1 + T_e / T_{ion})$. As the thermal equilibrium condition i.e $T_h = T_e = T_{ion}$ was applied thus, $D_a \cong 2D_{ion}$.

2.2 Particle model

The following assumptions are made in the analysis of plasma-particle interactions in the ITP torch; the particle motion is two-dimensional, only the viscous drag force and gravity affect the motion of an injected particle, the temperature gradient inside the particle is neglected, and the particle charging effect caused by the impacts of electrons or positive ions is negligible. The particle charging effects have not been intensively studied yet. However, the electromagnetic drag forces caused by the particle charging of the injected particles are negligible compared with those by neutrals and charged particles due to negligible electrical conductivity of soda-lime-silica powders. Thus, the momentum equations for a single spherical particle injected vertically downward into the plasma torch can be expressed as follows:

$$\frac{du_p}{dt} = -\frac{3}{4} C_D \left(u_p - u\right) U_R \left(\frac{\rho}{\rho_p d_p}\right) + g \tag{8}$$

$$\frac{dv_p}{dt} = -\frac{3}{4} C_D \left(v_p - v\right) U_R \left(\frac{\rho}{\rho_p d_p}\right) \tag{9}$$

$$U_R = \sqrt{\left(u_p - u\right)^2 + \left(v_p - v\right)^2} \tag{10}$$

The particle temperature, liquid fraction and diameter are predicted according to the following energy balances:

$$Q = \pi d_p^2 h_c \left(T - T_p\right) - \pi d_p^2 \sigma_s \varepsilon \left(T_p^4 - T_a^4\right) \tag{11}$$

$$\frac{dT_p}{dt} = \frac{6Q}{\pi \rho_p d_p^3 C_{pp}} \quad \text{for } T_p < T_b \tag{12}$$

$$\frac{d\chi}{dt} = \frac{6Q}{\pi \rho_p d_p^3 H_m} \quad \text{for } 1000 \le T_p \le 1600 \tag{13}$$

$$\frac{dd_p}{dt} = \frac{2Q}{\pi \rho_p d_p^2 H_v} \quad \text{for } 1000 \le T_p \le 1600,\ T_p \ge T_b \tag{14}$$

Drag coefficient C_{Df} is calculated using Eq. (15) and the property variation at the particle surface layer and the non-continuum effects are taken into account by Eq. (16) and (17) [Chen, 1983].

$$C_{D\mathbf{f}} = \begin{cases} \dfrac{24}{R_e} & R_e \le 0.2 \\ \dfrac{24}{R_e}\left(1 + \dfrac{3}{16} R_e\right) & 0.2 < R_e \le 0.2 \\ \dfrac{24}{R_e}\left(1 + 0.11 R_e^{0.81}\right) & 2.0 < R_e \le 21.0 \\ \dfrac{24}{R_e}\left(1 + 0.189 R_e^{0.62}\right) & 21.0 < R_e \le 200 \end{cases} \tag{15}$$

$$f_1 = \left(\frac{\rho_\infty \mu_\infty}{\rho_s \mu_s}\right)^{-0.45} \tag{16}$$

$$f_2 = \left\{1 + \left(\frac{2-\alpha}{\alpha}\right)\left(\frac{\gamma}{1+\gamma}\right)\frac{4}{Pr_s} Kn\right\}^{-0.45}, \quad 10 - 2 < Kn < 0.1 \tag{17}$$

$$C_D = C_{D\mathbf{f}} f_1 f_2 \tag{18}$$

To take into account the steep temperature gradient between plasma and particle surface, the Nusselt correlation can be expressed by Eq. (19) [Lee, 1985]. The non-continuum effect is taken into account by Eq. (20) [Chen, 1983].

$$Nu_{\mathbf{f}} = \left(2.0 + 0.6 R_{e\mathbf{f}}^{1/2} Pr_{\mathbf{f}}^{1/3}\right)\left(\frac{\rho_\infty \mu_\infty}{\rho_s \mu_s}\right)^{0.6}\left(\frac{C_{p\infty}}{C_{ps}}\right)^{0.38} \tag{19}$$

$$f_3 = \left\{1 + \left(\frac{2-\alpha}{\alpha}\right)\left(\frac{\gamma}{1+\gamma}\right)\frac{4}{Pr_s} Kn\right\}^{-1}, \quad 10-3 < Kn < 0.1 \tag{20}$$

The convective heat transfer coefficient is predicted as follows:

$$h_c = \frac{\kappa_{\mathbf{f}}}{d_p} Nu_{\mathbf{f}} f_3 \tag{21}$$

2.2.1 Particle source terms

Let us assume Nt0 be the total number of particles injected per unit time, nd is the particle size distribution, and nr is the fraction of Nt0 injected at each point through the injection nozzle. Thus, the total number of particles per unit time traveling along the trajectory (l, k) corresponding to a particle diameter dl injected at the inlet point rk is:

$$N^{(l,k)} = n_{d_l} n_{r_k} N_t^0 \tag{22}$$

For the sake of computation, the particle concentration nr in the inlet is assumed to be uniform and to be separated into five injection points, which are at radial positions of 0.3, 0.45, 0.6, 0.75 and 0.9 mm. In the present computation the particles diameter distribution is assumed to be Maxwellian (similar to experiment). The particle size and corresponding distribution fraction are presented in Table 2. In the present computation, the powder is assumed to be composed of seven size particles according to its diameter and deviation. The average particle diameter is 58 μm and the maximum deviation is 67%. As a result, there are 35 different possible trajectories of the injected particles. The injection velocity of the particles is assumed to be equal to the injection velocity of carrier gas.

Particle diameter (μm)	20	40	50	68	77	80	90
Fraction	0.03	0.07	0.1	0.6	0.1	0.07	0.03

Table 2. Particle size and corresponding distribution fraction

To take into account the particles loading effects, particles source terms for the mass, momentum, energy and species conservation equations have been calculated in the same fashion as described in reference [Proulx, 1985], using the Particle-Source-In Cell (PSI-CELL) approach [Crowe,1977], where the particles are regarded as sources of mass, momentum and energy. The source terms in the mass and species conservation equation, S_p^C is the net efflux rate of particles mass in a computational cell (control volume). Assuming the particles

are spherical, the efflux rate of particle mass for the particle trajectory (l, k) that traverses a given cell (i, j) is:

$$S_{p,ij}^{C(l,k)} = \frac{1}{6}\pi\rho_p N_{ij}^{(l,k)}\left(d_{ij,in}^3 - d_{ij,out}^3\right) \tag{23}$$

The net efflux rate of particle mass is obtained by summing over all particles trajectories which traverse a given cell (i, j):

$$S_{p,ij}^{C} = \sum_l \sum_k S_{p,ij}^{C(l,k)} \tag{24}$$

The source terms for momentum conservation equations are evaluated in the same fashion as that of mass conservation equation. In this case, the efflux rate of particles momentum for the particle trajectory (l, k) traversing a given cell (i, j) is:

$$S_{p,ij}^{M_z(l,k)} = \frac{1}{6}\pi\rho_p N_{ij}^{(l,k)}\left(u_{ij,in}d_{ij,in}^3 - u_{ij,out}d_{ij,out}^3\right) \tag{25}$$

$$S_{p,ij}^{M_r(l,k)} = \frac{1}{6}\pi\rho_p N_{ij}^{(l,k)}\left(v_{ij,in}d_{ij,in}^3 - v_{ij,out}d_{ij,out}^3\right) \tag{26}$$

Thus, the corresponding source terms for axial and radial momentum conservation equations are:

$$S_{p,ij}^{M_z} = \sum_l \sum_k S_{p,ij}^{M_z(l,k)} \tag{27}$$

$$S_{p,ij}^{M_r} = \sum_l \sum_k S_{p,ij}^{M_r(l,k)} \tag{28}$$

The source term for energy conservation equation $S_{p,ij}^{E}$ consists of the heat given to the particles $Q_{p,ij}^{(l,k)}$, and superheat to bring the particle vapors into thermal equilibrium with the plasma $Q_{v,ij}^{(l,k)}$:

$$Q_{p,ij}^{(l,k)} = \int_{\tau_{in}}^{\tau_{out}} \pi d_p^2 h_c\left(T_{ij} - T_{p,ij}^{(l,k)}\right)dt \tag{29}$$

$$Q_{v,ij}^{(l,k)} = \int_{\tau_{in}}^{\tau_{out}} \frac{\pi}{2}\pi d_p^2\rho_p\left(\frac{dd_p}{dt}\right)C_{pv}\left(T_{ij} - T_{p,ij}^{(l,k)}\right)dt \tag{30}$$

$$S_{p,ij}^{E} = \sum_l \sum_k N_{ij}^{(l,k)}\left(Q_{p,ij}^{(l,k)} + Q_{v,ij}^{(l,k)}\right) \tag{31}$$

The calculation is started by solving the plasma temperature and flow fields without injection of any particles. Using these conversed temperature and flow fields, particles trajectories together with particle temperature and size histories are calculated. The particle

source terms for the mass, momentum and energy conservation equations for each control volume throughout the torch are then predicted. The plasma temperature and flow fields are predicted again incorporating these particle source terms. The new plasma temperature and flow fields are used to recalculate the particles trajectories, temperature and size histories. Calculating the new source terms and incorporating them into conservation equations constitute the effects of plasma-particle interaction, thereby completing the cycle of mutual interaction. The above computation schemes are repeated until convergence. The physical properties of soda-lime-silica glass powders used in the present investigation are listed in Table 3.

Mass density	2300 kg/m^3
Specific heat at constant pressure	800 J/kg-K
Porosity	80%
Fusion temperature	1000~1600 K
Boiling temperature	2500 K
Latent heat of fusion	3.69×10^5 J/kg
Latent heat of vaporization	1.248×10^7 J/kg

Table 3. Physical properties of soda-lime-silica glass powders

3. Simulated results

The calculation has been carrier out for a plasma power of 10 kW, reactor pressure 0.1 MPa and induction frequency 4 MHz. The discharge conditions are tabulated in Table 1. In this study, attention is given to the plasma-particle interaction effects on individual particle trajectory, velocity, and temperature history along the trajectories for different carrier gas flow-rate and powder feed-rates. Attention also paid to investigate how the plasma-particle energy exchange process is affected by the particle loading effects. Two aspects of the thermal treatment are investigated: the behavior of the individual particles, and the global effects of the particles on the plasma fields. The carrier gas flow-rate is very vital in determining the individual particle trajectories, and the allowable powder feed-rate. Figure 2 shows the isotherms in the torch for a carrier gas flow-rate of 6 L/min argon and various powder feed-rates. The other discharge conditions are the same as presented in Table 1. A comparison among the isotherms clearly reveals the intense cooling around the torch centerline that increases with powder feed-rate. However, the plasma temperature away from the centerline of the torch remains almost unaffected by higher powder feed-rates. This is because the
individual particle trajectories are not widely outbound in the radial direction; rather the trajectories are very close to the torch axis. Thus, the plasma-particle interaction around the centerline is very crucial at higher powder feed-rate. The same kind of arguments is proposed by Ye et al [Ye, 2000] to explain the particle trajectories for alumina and tungsten particles. The effects of carrier gas flow-rates on the individual particle trajectories are presented in Fig. 3, for the particle diameter of 50 μm and a feed-rate of 5 g/min. It is comprehended that the higher flow-rate of carrier gas enhances the axial velocity of the particles, because the initial axial velocity of the particles depends on carrier gas flow rate; as a result the trajectories become closer to the torch axis at higher flow-rate. The individual particle temperature history along the trajectory is also influenced by the carrier gas flow-

rate and powder feed-rate. Figure 4 shows the effects of carrier gas flow-rate on the particle temperature for a feed-rate of 5 g/min. It is found that the particle temperature along the trajectory decreases at higher carrier gas flow-rate. The main reason is the cooling of plasma at Fig. 2 Effects of powder loading on the isotherms for a carrier gas flow-rate of 6 L/min higher carrier gas flow-rate that leads less heat transfer to particles. Figure 5 describes the effects of powder feed-rate on the particle temperature along the trajectory. Like the flow-rate of carrier gas, the higher feed-rate of powder also causes intense cooling of plasma; thus, the heat transfer to particles decreases what results lower particle temperature. At this stage of investigation, it is indeed necessary to discuss the energy transfer mechanism to particles. The energy transfer is affected by the particles physical properties, plasma temperature, and velocity. The last two parameters are affected to a large extent by the carrier gas flow-rate and powder loading. The net energy transfer to particles is calculated by integrating the energy transfer rate to the particles injected per unit time over the residence time for all the particle trajectories. Mathematically the net energy transfer to particles (Q_{net}) can be expressed as follows:

$$Q_t = \int_{t=0}^{t=t_s} \left\{ \pi d_p^2 h_c \left(T - T_p \right) - \pi d_p^2 \sigma_s \varepsilon \left(T_p^4 - T_a^4 \right) \right\} dt \tag{32}$$

$$Q_{net} = \sum_l \sum_k N^{(l,k)} Q_t \tag{33}$$

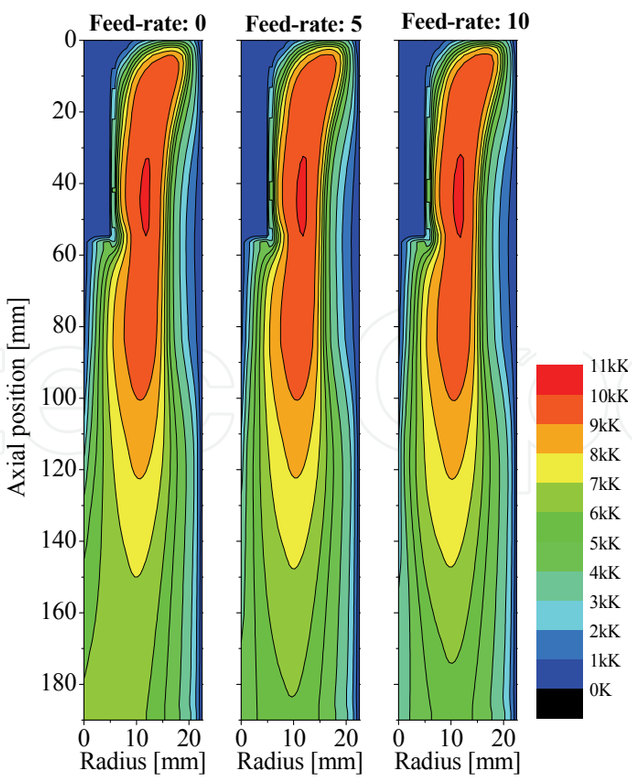

Fig. 2. Effects of powder loading on the isotherms for a carrier gas flow-rate of 6 L/min

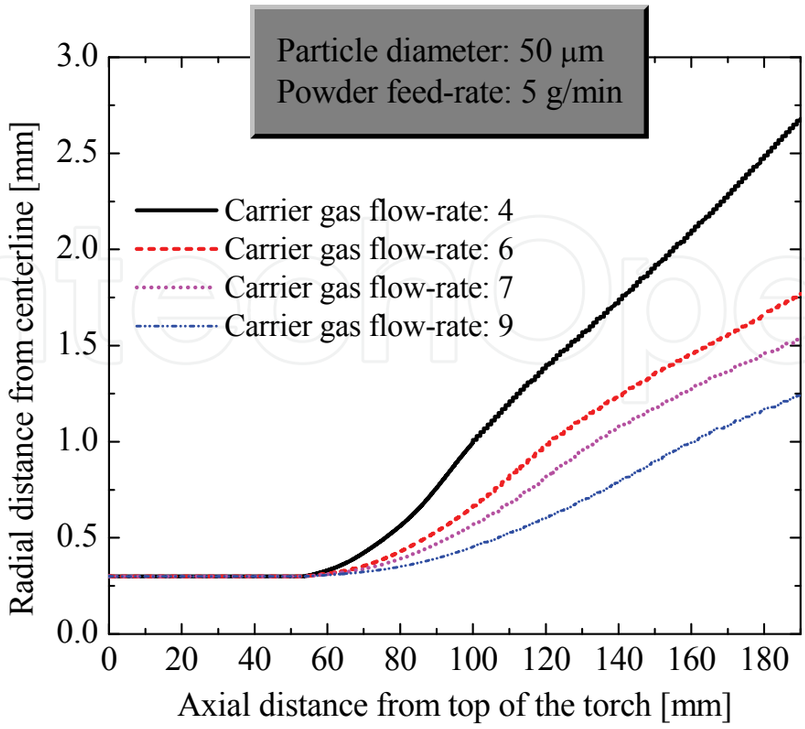

Fig. 3. Effects of carrier gas flow-rate on the particle trajectories for a powder feed-rate of 5 g/min

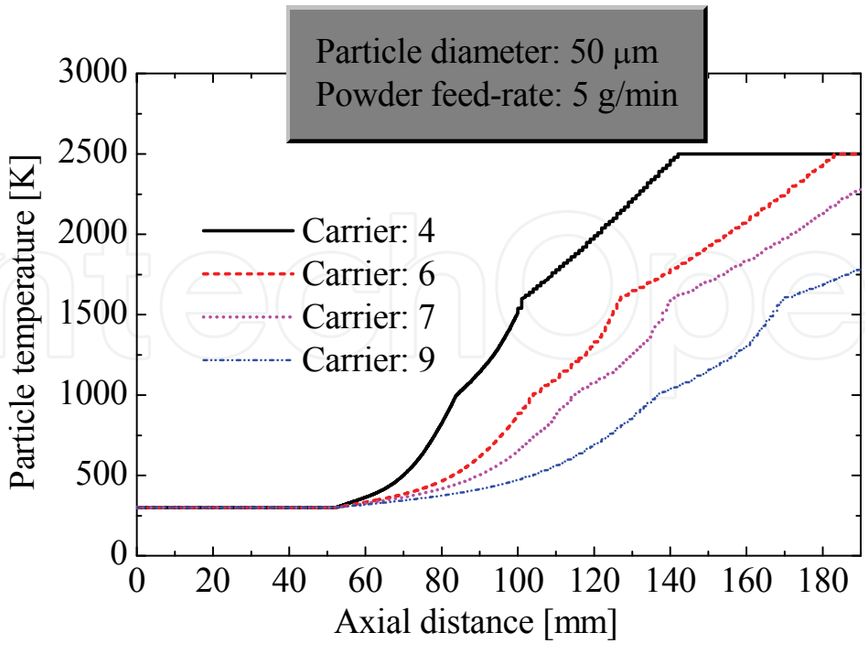

Fig. 4. Dependence of particle temperature history along the trajectory on carrier gas flow-rate

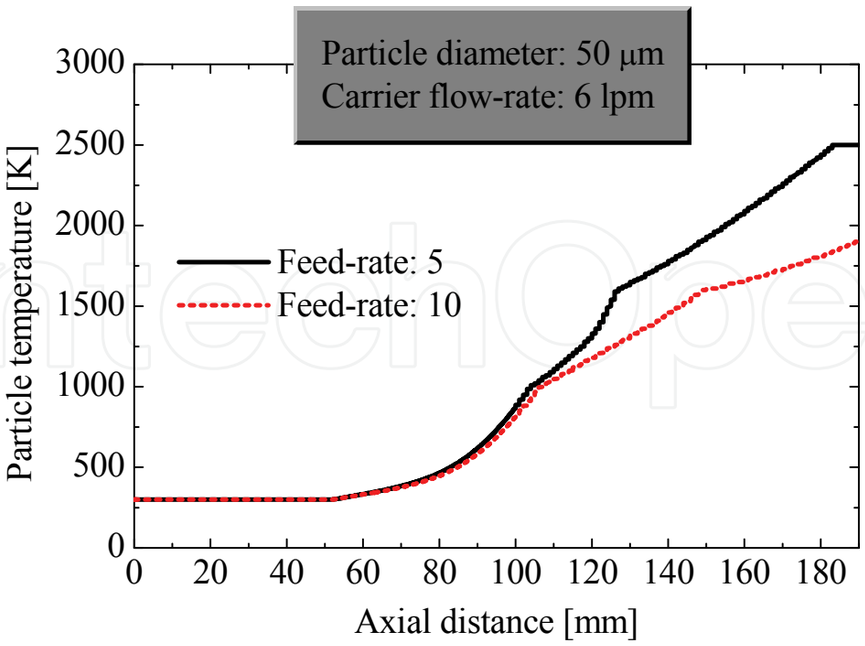

Fig. 5. Dependence of particle temperature history along the trajectory on the powder feed-rate

Figure 6 clearly presents how the net energy transfer to particles is affected by the carrier gas flow-rate under powder loading conditions. Only 5 g/min of powder feeding decreases

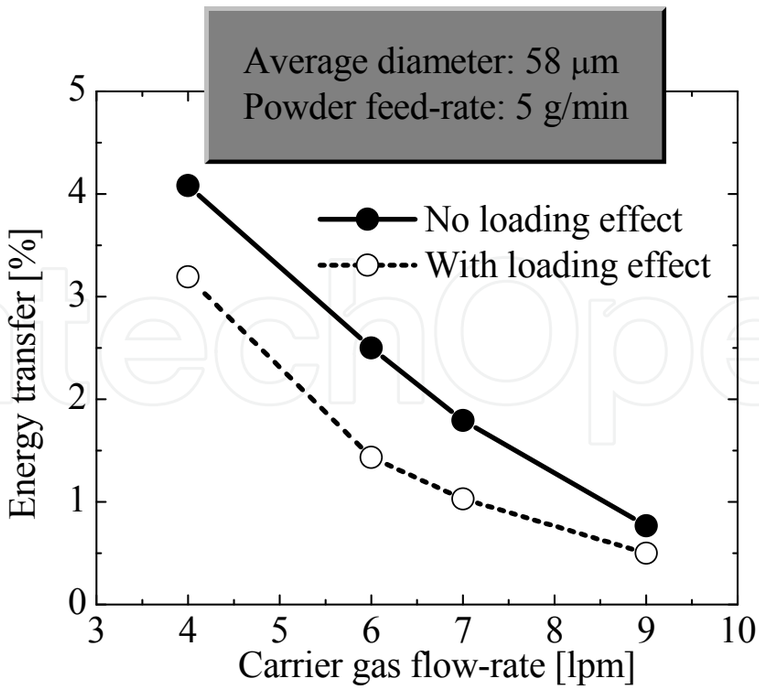

Fig. 6. Effects of powder loading and carrier gas flow-rate on the plasma-particle energy transfer

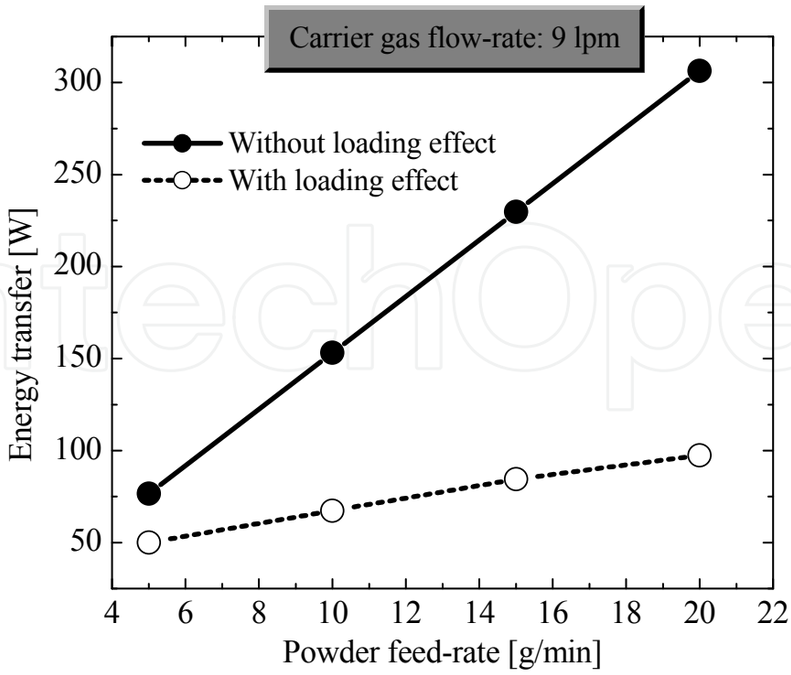

Fig. 7. Particle loading effects on plasma-particle energy transfer at various powder feed-rate

the energy transfer to particle by about 44%. The powder loading effect and the dependence of energy transfer to particles on the powder feed-rate is presented in Fig. 7, for a carrier gas flow-rate of 9 L/min. It can be noticed that energy transfer to particles increases linearly with feed-rate in the absence of particle loading effect; however, when particle loading effect is taken into account, energy transfer to particles yet increases with feed-rate but with a declined slop. The main reason is the intense local cooling of plasma around the torch centerline under dense particle loading. It is also evident that the particle loading effect is pronounced at higher powder feed-rate.

4. Experimental

4.1 Setup

The experimental setup consists of a plasma torch (Fig. 1), a reaction chamber, powder feeder, and a power supply unit (4 MHz, 20 kW). The plasma torch consists of a water-cooled co-axial quartz tube surrounded by a three-turn induction coil. The granulated soda-lime-silica glass powders are prepared by spray-drying method from the reagents of Na_2CO_3, $CaCO_3$ and SiO_2 with the composition of Na_2O:16, CaO:10 and SiO_2:74 in wt%. The mean diameter and porosity of soda-lime-silica glass powders are 58 μm and 80%, respectively. The plasma discharge conditions are the same as those described in Table 1 in the modeling section. The soda-lime-silica glass powders are injected into ITP torch along with the carrier gas at a rate of 5-20 g/min and the quenched powders are collected on a water-cooled ceramic block at 340 mm from the nozzle exit.

4.2 Characterization of plasma-treated particles

The treatment quality of the powders is characterized by the vitrification degree, the surface morphology, cross-sectional structure and composition of the quenched powders. The

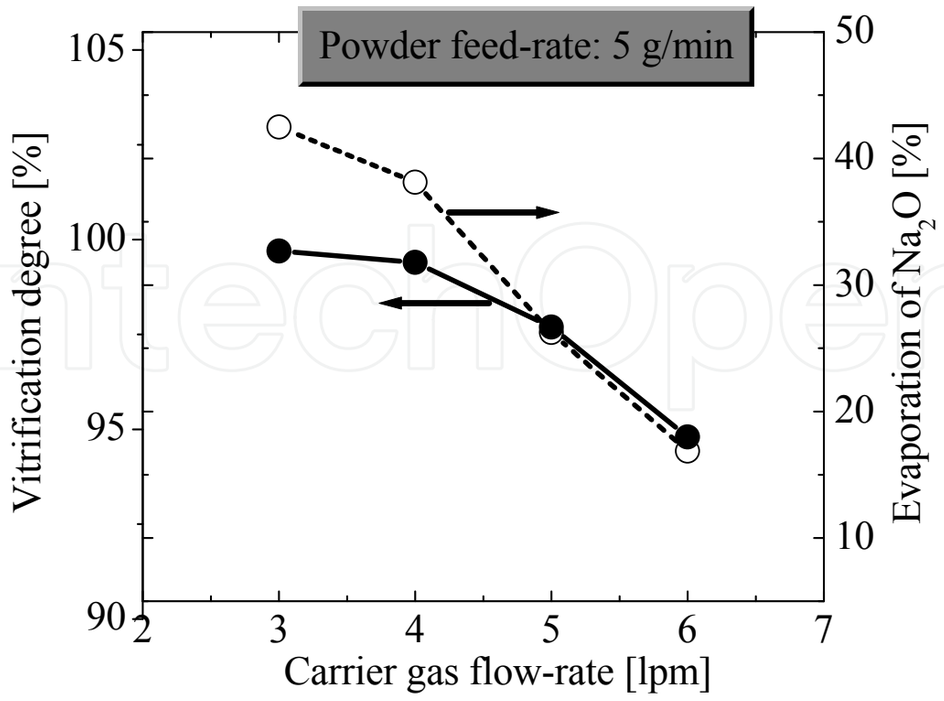

(a)

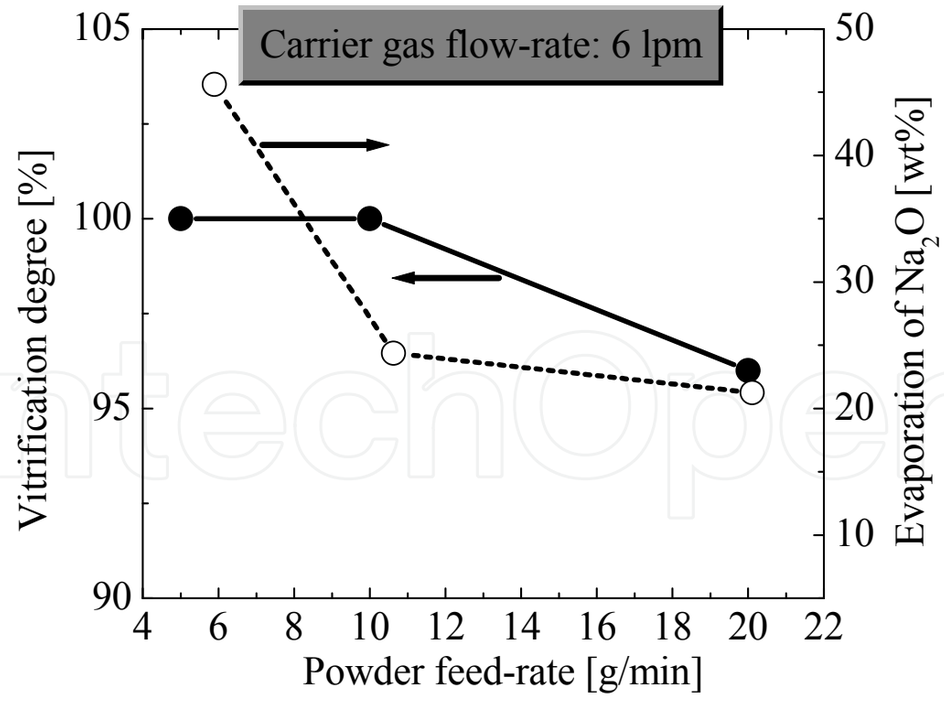

(b)

Fig. 8. Effects of carrier gas flow-rate (a), and powder feed-rate (b) on the vitrification degree and Na_2O evaporation rate

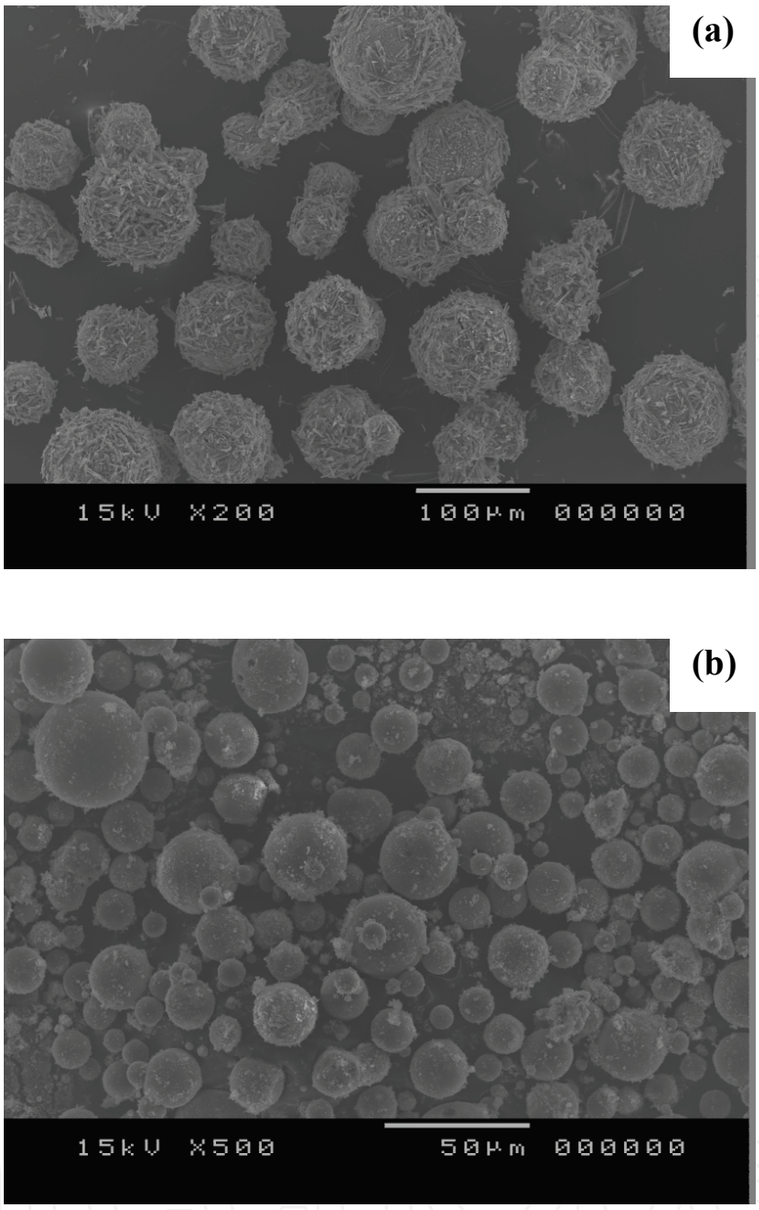

Fig. 9. The SEM photographs of soda-lime-silica glass powders before (a), and after (b) thermal treatment

vitrification degree is defined as the ratio of the converted crystalline phases of SiO_2 in the quenched powder to the crystalline SiO_2 in the raw powders. The vitrification degree of quenched powders is quantitatively determined by X-ray diffractometry (XRD) on Miniflex (Rigaku) with Cu Kα radiation at 30 kV and 15 mA. The data are collected in the 2θ range 3-90° with a step size of 0.02° and a scan speed of 4°/min. The quenched powders collected at the reaction chamber are examined by scanning electron microscopy (SEM) on JSM5310 (JEOL) to observe their surface morphologies and cross-sectional microstructures. The composition of quenched powders is analyzed by inductively coupled plasma (ICP) on ICP-8100 (SHIMADZU).

4.3 Experimental results

In the experiment soda-lime-silica glass powders are injected along with the carrier gas through the nozzle inserted into the plasma torch. Thus, the initial particle velocity is the same as that of carrier gas. When the particles come in contact to high temperature plasma flame, they are heated and their temperature starts to rise. As the particle temperature reaches to its melting temperature, particle porosity decreases drastically; as a result, particle diameter shrinks. When particle temperature reaches to its boiling temperature, vaporization takes place and particle diameter shrinks further. In order to investigate the effects of carrier gas flow-rate and powder feed-rate on energy transfer to particles, the vitrification degree and Na_2O evaporation rate are estimated through XRD and ICP spectrum analysis. Higher vitrification degree and Na_2O evaporation rate indirectly indicate the large energy transfer to particles. Figure 8 shows the XRD and ICP spectrum analysis results. It can be noticed that both the evaporation rate of Na_2O and the vitrification degree decrease with the increase of both carrier gas flow-rate [Fig. 8(a)] and powder feed-rate [Fig. 8(b)]. The vitrification degree and the evaporation of Na_2O depend to a large extent on the particle temperature. Higher carrier gas flow-rate and powder feed-rate cause lower plasma temperature which causes less heat transfer to particles; as a result particle temperature is lower. It is important to underline that after the thermal treatment, the size, composition, and morphology of the particles have been changed significantly. The effects of thermal treatment are visualized in the SEM photograph as shown in Fig. 9. From Fig. 9 (a) and (b), it can be noticed that after treatment, the particle size becomes smaller, quite spherical, smoother and compact surface.

5. Discussions

To validate the modeling and simulated results, a comparative discussion between simulated and experimental results are indeed necessary. From the experimental results it is found that at higher carrier gas flow-rate and powder feed-rate, both the evaporation rate of Na_2O and the vitrification degree decrease. These results indicate that less heat transfer to particles takes place at higher carrier gas flow-rate and powder feed-rate. From the simulated results it is evident that at increased carrier gas flow-rate and powder feed-rate, the energy transfer to particles decreases; as a result, particles temperature becomes lower. It is convinced that the main reason of less heat transfer to particles is the severe local cooling of plasma around the torch centerline at higher carrier gas flow-rate and powder feed-rate. Thus, it may be argued that the simulated results well agree with the experimental findings.

6. Conclusions

In this chapter we basically, discussed the way of thermal treatment of any type of granulated porous particles by induction thermal plasma. A general plasma-particle interactive flow model has been discussed using what it is possible to simulate the particle trajectories, temperature histories, plasma temperature contours etc. The described model can be used to optimize the carrier gas flow-rate, particle size, and powder feed-rate to achieve the maximum treatment efficiency during thermal treatment of granulated powders by argon-oxygen induction thermal plasmas. Numerically, it is found that the heat transfer to particles decreases at increased carrier gas flow-rate and powder feed-rate, and these results well agree with those of experiment. Thus, it can be concluded that, efficient thermal

treatment of particles depends not only on the physical properties of the particles, but also on the plasma discharge conditions and particle parameters. Therefore, for a particular type of powder (certain physical properties) both carrier gas flow-rate and powder feed-rate mainly govern the treatment quality.

7. Nomenclature

A_c Complex amplitude of vector potential
B Magnetic field vector
C_p Specific heat at constant pressure
C_{pp} Particle specific heat at constant pressure
d_p Particle diameter
D_{ij} Binary diffusion coefficient between species i and j
D_m Multicomponent diffusion coefficient
E Electric field vector
f Frequency
g Acceleration of gravity
h Enthalpy
h_c Heat transfer coefficient
H_m Latent heat of melting
H_v Latent heat of vaporization
i Complex vector ($\sqrt{-1}$)
J Current density vector
K_n Knudsen number
M_i Molecular weight of species i
M_j Molecular weight of species of j
N_t^0 Total number of particles injected per unit time
n_d Particle size distribution
n_r Fraction of Nt0 injected at each point
Nu Nusselt number
p Pressure
Pr Prandtl number
Q Net heat exchange between the particle and its surroundings
Q_r Volumetric radiation loss
Re Reynold number
S_p^C Particle source term in continuity equation
S_p^M Particle source term in momentum equation
S_p^E Particle source term in energy equation
t Time
T Plasma temperature
T_a Ambient temperature
T_b Boiling point temperature of particles
T_e Electron temperature
T_h Heavy particle temperature
T_{ion} Ion temperature

T_p Particle temperature
t_s Residence time of particle in the plasma
u Velocity vector
u_p Axial velocity component of particle
U_R Relative speed of particles with respect to plasma
v_p Radial velocity component of particle
x_i Mole fraction of species i
y Mass fraction

Greek symbols

Vector operator
κ Thermal conductivity
Mass density
Viscosity
σ Electrical conductivity
κ Thermal conductivity
μ_0 Permeability of free space
ω Angular frequency ($2\pi f$)
$\bar{\Omega}_{ij}^{(1,1)}$ Collision integral between species i and j
ε Particle porosity
σ_s Stefan-Boltzmann constant
Liquid mass fraction of a particle
Thermal accommodation coefficient
γ Specific heat ratio

Subscripts

f Properties corresponding to film temperature
p Particle
s Properties corresponding to particle temperature
∞ Properties corresponding to plasma temperature
(i, j) Location of a control volume or cell

Superscripts

(l, k) Particles having an initial diameter d_l, and injection point r_k.

8. References

Boulos, M. I, 1978, "Heating of powders in the fire ball of an induction plasma," IEEE Trans. on Plasma Sci. PS-6, pp. 93-106.

Crowe, C. T., Sharma, M. P., and Stock, D. E., 1977, "The particle-source-in cell (PSI-CELL) model for gas-droplet flows," J. Fluid Eng., 99, pp. 325-332.

Chen, X., and Pfender, E., 1983, "Effects of Knudsen number on heat transfer to a particle immersed into a thermal plasma," Plasma Chem. Plasma Process., 3, pp. 97-113.

Fan, X., Ishigaki, T., and Sato, Y., 1997, "Phase formation in molybdenum disilicide powders during in-flight induction plasma treatment," J. Mater. Res., 12, pp. 1315-1326.

Mostaghimi, J., Paul, K. C., and Sakuta, T., 1998, "Transient response of the radio frequency inductively coupled plasma to a sudden change in power," J. Appl. Phys., 83, pp. 1898-1908.

Lee, Y. C., Chyou, Y. P., and Pfender, E., 1985, "Particle dynamics and particle heat and mass transfer in thermal plasmas. Part II. Particle heat and mass transfer in thermal plasmas," Plasma Chem. Plasma Process., 5, pp. 391-414.

Patankar, S. V., 1980, Numerical fluid flow and heat transfer, Hemisphere, New York.

Proulx, P., Mostaghimi, J., and Boulos, M. I., 1985, "Plasma-particle interaction effects in induction plasma modeling under dense loading conditions," Int. J. Heat Mass Transfer, 28, pp. 1327-1335.

Reed T. B. "Induction-Coupled Plasma Torch," *Journal of Applied Physics*, 1961, 32(5), p.821

Tanaka, Y., Paul, K. C., and Sakuta, T., 2000, "Thermodynamic and transport properties of N_2/O_2 mixtures at different admixture ratio," Trans. IEE Japan, 120-B, pp. 24-30.

Watanabe, T., and Fujiwara, K., 2004, "Nucleation and growth of oxide nanoparticles prepared by induction thermal plasmas," Chem. Eng. Comm., 191, pp. 1343-1361.

Yoshida, T., and Akashi, K., 1977, "Particle heating in a radio-frequency plasma torch," J. Appl. Phys., 48, pp. 2252-2260.

Ye, R., Proulx, P., and Boulos, M. I., 2000, "Particle turbulent dispersion and loading effects in an inductively coupled radio frequency plasma," J. Phys. D: Appl. Phys., 33, pp. 2154-2162.

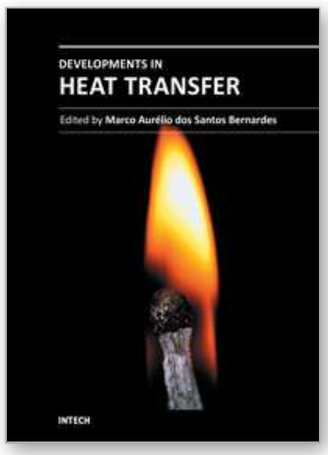

Developments in Heat Transfer

Edited by Dr. Marco Aurelio Dos Santos Bernardes

ISBN 978-953-307-569-3
Hard cover, 688 pages
Publisher InTech
Published online 15, September, 2011
Published in print edition September, 2011

This book comprises heat transfer fundamental concepts and modes (specifically conduction, convection and radiation), bioheat, entransy theory development, micro heat transfer, high temperature applications, turbulent shear flows, mass transfer, heat pipes, design optimization, medical therapies, fiber-optics, heat transfer in surfactant solutions, landmine detection, heat exchangers, radiant floor, packed bed thermal storage systems, inverse space marching method, heat transfer in short slot ducts, freezing an drying mechanisms, variable property effects in heat transfer, heat transfer in electronics and process industries, fission-track thermochronology, combustion, heat transfer in liquid metal flows, human comfort in underground mining, heat transfer on electrical discharge machining and mixing convection. The experimental and theoretical investigations, assessment and enhancement techniques illustrated here aspire to be useful for many researchers, scientists, engineers and graduate students.

INTECH
open science | open minds

InTech Europe
University Campus STeP Ri
Slavka Krautzeka 83/A
51000 Rijeka, Croatia
Phone: +385 (51) 770 447
Fax: +385 (51) 686 166
www.intechopen.com

InTech China
Unit 405, Office Block, Hotel Equatorial Shanghai
No.65, Yan An Road (West), Shanghai, 200040, China
中国上海市延安西路65号上海国际贵都大饭店办公楼405单元
Phone: +86-21-62489820
Fax: +86-21-62489821

IntechOpen